Strain-induced quasi-one-dimensional rare-earth silicide structures on Si(111)

F. Timmer,[1,2] R. Oelke,[1,2] C. Dues,[3] S. Sanna,[3] W. G. Schmidt,[3] M. Franz,[4] S. Appelfeller,[4] M. Dähne,[4] and J. Wollschläger[1,2,*]

[1]*Fachbereich Physik, Universität Osnabrück, Barbarastraße 7, 49069 Osnabrück, Germany*

[2]*Center of Physics and Chemistry of New Materials, Barbarastraße 7, 49069 Osnabrück, Germany*

[3]*Lehrstuhl für Theoretische Physik, Universität Paderborn, Warburgerstr. 100, 33095 Paderborn, Germany*

[4]*Institut für Festkörperphysik, Technische Universität Berlin, Hardenbergstraße 36, 10623 Berlin, Germany*

(Received 14 July 2016; revised manuscript received 1 October 2016; published 28 November 2016)

After deposition of rare-earth elements (Dy, Tb) on Si(111) at elevated temperatures, a formerly unknown $(2\sqrt{3} \times \sqrt{3})R30^\circ$ reconstruction is observed by low-energy electron diffraction, while scanning tunneling microscopy measurements exhibit a $(\sqrt{3} \times \sqrt{3})R30^\circ$ reconstruction. On the basis of density-functional theory calculations, the structure of the larger unit cell is explained by periodically arranged subsurface Si vacancies. The vacancy network in the first subsurface layer has a $(\sqrt{3} \times \sqrt{3})R30^\circ$ periodicity, while strain is released by a $(2\sqrt{3} \times \sqrt{3})R30^\circ$ Si vacancy network in the second subsurface layer. In addition, this vacancy network forms quasi-one-dimensional structures (striped domains) separated by periodically arranged antiphase domain boundaries. The diffraction spot profiles are explained in detail by kinematic diffraction theory calculations, and average domain widths are deduced.

DOI: 10.1103/PhysRevB.94.205431

I. INTRODUCTION

The growth of rare earths (REs) on Si surfaces leads to the formation of silicide structures, which have been a focus of research for more than 30 years due to their unique properties [1–4].

On the (001) surface and its vicinal surfaces, the RE silicides do not form planar films due to an anisotropic lattice mismatch, and instead quasi-one-dimensional structures (nanowires) can be grown [5,6]. Such nanowires might be applicable as interconnects in future nanodevices [7] or as plasmonic waveguides [8] due to their quasi-one-dimensional structure.

On the (111) surface, in contrast, the lateral lattice mismatch between silicide and Si substrate is very small, and planar RE silicide films can be grown epitaxially. Most trivalent rare-earth elements (REEs) form silicide layers with very similar structural and electronic properties. Depending on the amount of REEs deposited and the thermal formation conditions, a plethora of reconstructions has been observed. In the submonolayer regime, the quasi-one-dimensional (5×2) as well as the two-dimensional $(2\sqrt{3} \times 2\sqrt{3})R30^\circ$ reconstructed films can be observed on the Si(111) surface [9–15]. The two-dimensional $RESi_2$ film with (1×1) periodicity is found at coverages around one monolayer (ML), and at higher coverages the multilayer $(\sqrt{3} \times \sqrt{3})R30^\circ$ reconstruction can be observed, consisting of alternating layers of REEs and Si atoms with an RE_3Si_5 stoichiometry for the silicide bulk and a periodic arrangement of Si vacancies [1,3,9,13–15]. Moreover, these monolayer and multilayer films are characterized by an abrupt interface as well as low Schottky-barrier heights on *n*-type Si(111), making them interesting for Ohmic contacts on *n*-type Si or photovoltaics and photodetectors on *p*-type Si [2,16].

Here, we report on the deposition of Dy and Tb on Si(111) at elevated temperatures. Both RE silicides form a $(2\sqrt{3} \times \sqrt{3})R30^\circ$ reconstruction. This structure is observed for REE coverages up to several ML and shows a rather smooth surface, so that it can be related to the $(\sqrt{3} \times \sqrt{3})R30^\circ$ and not to the submonolayer $(2\sqrt{3} \times 2\sqrt{3})R30^\circ$ reconstruction. The structure of the silicide films is characterized by means of low-energy electron diffraction (LEED), including spot profile analysis (SPA-LEED), scanning tunneling microscopy (STM), and density-functional theory (DFT). Additionally, the stoichiometry of the films and their growth mode is studied by Auger electron spectroscopy (AES). It is demonstrated that this superstructure forms quasi-one-dimensional structures, due to the formation of striped antiphase domains, and a detailed structure model will be presented.

II. METHODOLOGY

A. Experimental

The experiments are conducted in two different experimental setups using two different REEs (Dy,Tb). One of the setups is equipped with a SPA-LEED system and an AES system, while the other one is equipped with an STM and a conventional LEED system.

In both chambers, the Si(111) substrates are prepared by degassing for 12 h at 600 °C until the base pressure is smaller than 2×10^{-10} mbar. Subsequently, the substrates are flash-annealed at 1150 °C several times, while maintaining a pressure smaller than 2×10^{-9} mbar to remove the native oxide and to obtain the well-known (7×7) reconstruction. The pristine condition of the substrate is confirmed via SPA-LEED and AES in the first chamber, while LEED and STM are used for this purpose in the second chamber. The REEs are deposited via molecular-beam epitaxy at 650 °C ($p \leqslant 2 \times 10^{-9}$ mbar), and their exposure is controlled by a flux monitor calibrated via AES in the first chamber and by a quartz crystal microbalance in the second chamber. Coverages are given in monolayers, where 1 ML corresponds to one RE atom per Si(111) unit cell, i.e., an area density of 7.83×10^{14} cm^{-2}. The temperatures are

*Corresponding author: jwollsch@uos.de

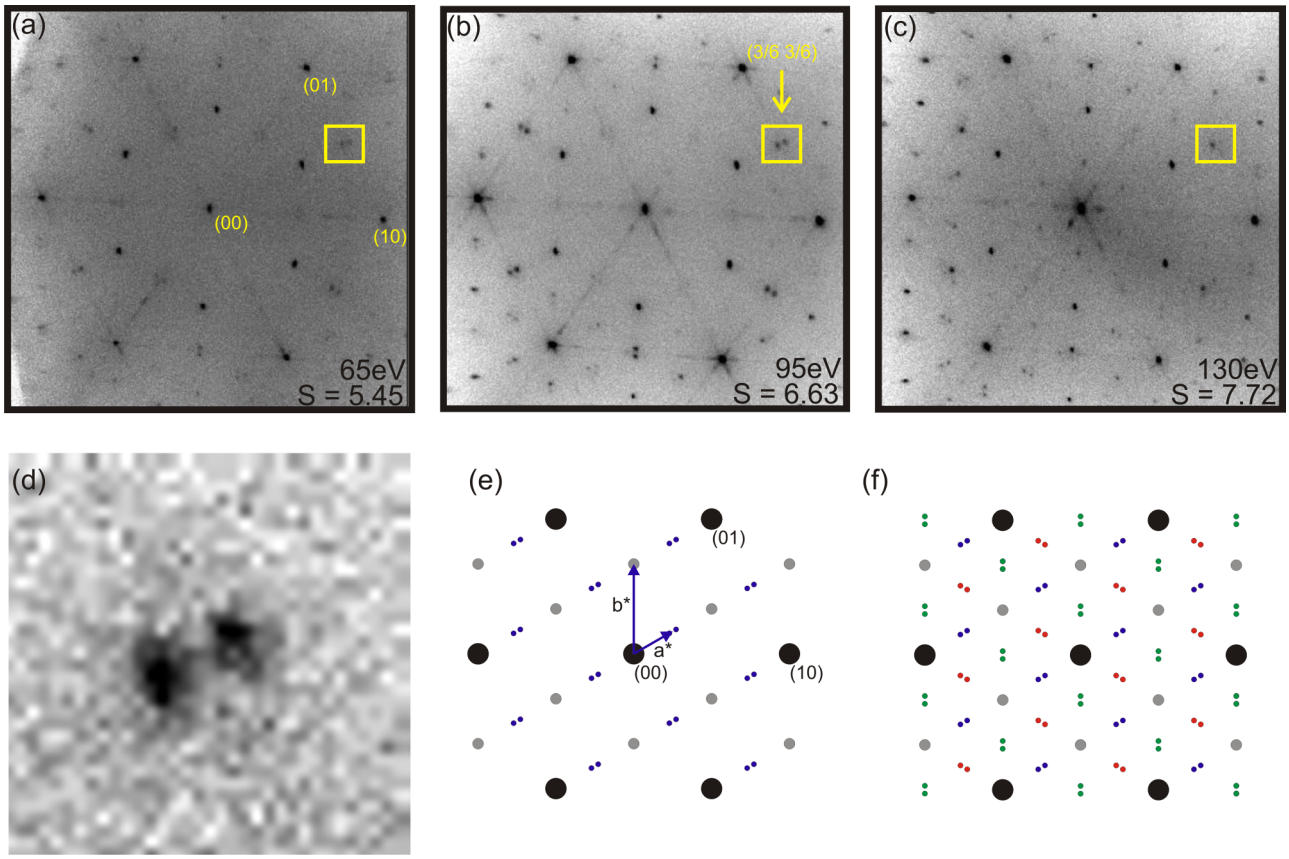

FIG. 1. (a)–(c) Observed $(2\sqrt{3} \times \sqrt{3})R30^\circ$ SPA-LEED patterns with three rotational domains after deposition of 2 ML Dy at 650 °C, shown for different electron energies and corresponding scattering phases $E = (65,95,130\ \text{eV}) \equiv S = (5.45,6.63,7.72)$. The scattering phase $S = \frac{2c}{\lambda_{el}}$ is a measure for the interference condition between adjacent layers in a crystal. Here, λ_{el} and c denote the de Broglie wavelength of the electrons and the layer spacing, respectively. Integer values of S indicate constructive interference, whereas values of $S = n + 0.5$ ($n \in \mathbb{N}$) indicate destructive interference. The layer distance equates to $c = 4.15$ Å for the silicide model that is derived in this work. Here, a scattering phase of $S = 1$ corresponds to $k_\perp = 1.51\ \text{Å}^{-1}$. Some of the $(2\sqrt{3} \times \sqrt{3})R30^\circ$ diffraction spots are split, as indicated by the yellow boxes. (d) Magnification of the yellow box in (b) showcasing the spot splitting of the third-order diffraction spot $[(h,k) = (3/6,3/6)]$. (e),(f) Schematic description of the experimentally observed diffraction pattern. The diffraction pattern of a single domain is shown in (e), and the diffraction pattern of all three rotational domains is shown in (f). Every diffraction spot of odd order in the direction of the $2\sqrt{3}$ periodicity is split.

monitored with infrared pyrometers. To prevent contamination effects after preparation, the samples were immediately cooled down for ∼30 min and directly analyzed *in situ* by means of (SPA-)LEED and STM.

B. Computational

Silicide thin films are modeled within the DFT, as implemented in the Vienna ab initio simulation package (VASP) [17,18]. Thereby, we perform total-energy calculations within the generalized gradient approximation (GGA) in the Perdew-Burke-Ernzerhof (PBE) formulation [19,20]. Projector augmented wave (PAW) potentials [21,22] with projectors up to $l = 1$ for H, $l = 2$ for Si, and $l = 3$ for the RE atoms are used. One $(1s^1)$, four $(3s^2 3p^2)$, and nine $(5d^1 5p^6 6s^2)$ valence electrons are employed for the simulation of H, Si, and the RE atoms, respectively. As no valence state other than RE^{3+} has been observed for the RE ions in the silicide structures, we constrain the valence state of the investigated REEs (frozen-core method). This approach allows for a proper treatment of the lanthanides within DFT [23–25]. In our models, we consider Tb and Dy (atomic numbers 65 and 66) as prototypical trivalent REEs. However, our experience with other silicide structures [9] shows that the results may be extended, at least qualitatively, to all trivalent REEs. The electronic wave functions are expanded into plane waves up to an energy cutoff of 400 eV. A $12 \times 12 \times 1$ Monkhorst-Pack [26] k-point mesh was used for the simulation of the structure with $2\sqrt{3} \times \sqrt{3}$ periodicity. The silicide surfaces are modeled with asymmetric slabs consisting of six Si bilayers stacked along the [111] crystallographic direction modeling the substrate, the silicide thin film, and a vacuum region of at least 15 Å. Hydrogen atoms saturate the dangling bonds at the lower face of the slabs. The supercells modeling the silicide monolayer structure with 1×1 periodicity contain one Tb or Dy atom and are described in detail in [9]. Supercells modeling the silicide trilayer structure with $2\sqrt{3} \times \sqrt{3}$ periodicity contain 18 rare-earth atoms and are illustrated in detail in Sec. III B. The atomic positions are relaxed until the residual Hellmann-Feynman forces are lower than 0.001 eV/Å. The three lower Si bilayers and the hydrogen atoms are kept constrained in order to model the substrate, while the silicide

film and the upper three Si bilayers are free to relax. Dipole-correction algorithms have been used to correct the spurious interactions of the slabs with their periodic images [27,28]. Thus, our calculations are on the same footing as our previous investigation of silicide thin films of different periodicity [9].

III. RESULTS AND DISCUSSION

A. Structure: Experimental results

After deposition of 2–3 ML Dy at 650 °C sample temperature, the SPA-LEED patterns presented in Figs. 1(a)–1(c) are observed. At first glance, these patterns are reminiscent of the well-known $(2\sqrt{3} \times 2\sqrt{3})R30^\circ$ superstructure. However, upon closer inspection, a splitting of certain diffraction spots becomes visible [Fig. 1(d)]. The way the diffraction spots are split is in stark contrast to the situation that would be expected for a $(2\sqrt{3} \times 2\sqrt{3})R30^\circ$ periodicity. It will be demonstrated in the following that the surface is reconstructed with a $(2\sqrt{3} \times \sqrt{3})R30^\circ$ periodicity and has regularly arranged antiphase domain boundaries (APDBs).

In Fig. 1(e), the pattern of a single rotational domain is displayed schematically. It is found that only those diffraction spots are split that are described by $\mathbf{k}_\parallel = h\mathbf{a}^* + k\mathbf{b}^*$ with odd values of h. Here, $\mathbf{a}^*$ denotes the reciprocal base vector due to the $2\sqrt{3}$ periodicity, while $\mathbf{b}^*$ denotes the reciprocal base vector due to the $\sqrt{3}$ periodicity. The intensity ratio within a pair of split spots as well as the intensity ratio of first-order to third-order diffraction spots is a function of electron energy and thus of out-of-plane momentum, as will be explained in detail below. Additionally, the absolute intensity of diffraction spots varies as a function of electron energy as well [compare intensities of same order spots in Figs. 1(a)–1(c)]. This is most likely due to interference effects, which could only be explained in the context of the dynamical scattering theory (but is not considered in this paper). In Fig. 1(f), the superposition of the three rotational domains is shown, which is in nice agreement with the SPA-LEED patterns in Figs. 1(a)–1(c).

Detailed STM studies with atomic resolution are performed to shed light on the atomic structure of the $(2\sqrt{3} \times \sqrt{3})R30^\circ$ structure. Besides small patches covered with the $(2\sqrt{3} \times 2\sqrt{3})R30^\circ$ submonolayer structure, most of the surface appears as shown in Fig. 2 (here shown for the case of Tb). However, no indication for a $(2\sqrt{3} \times \sqrt{3})R30^\circ$ periodicity can be observed by STM, although LEED patterns very similar to those presented in Fig. 1 were observed (see below). Instead, the structure appears analogous to the well-known $(\sqrt{3} \times \sqrt{3})R30^\circ$ structure of the multilayer silicide on Si(111) [15]. The latter is explained by a periodically arranged Si vacancy network in the subsurface layer(s) leading to stress reduction and an RE_3Si_5 stoichiometry in the silicide bulk. However, for the samples prepared here, two different types of domains of the $(\sqrt{3} \times \sqrt{3})R30^\circ$ are present, which are composed of two different types of structure motifs (indicated by green triangles and red hexagons; see Fig. 2). These structure motifs correspond to different positions of the buckled silicide surface layer with respect to the Si vacancies

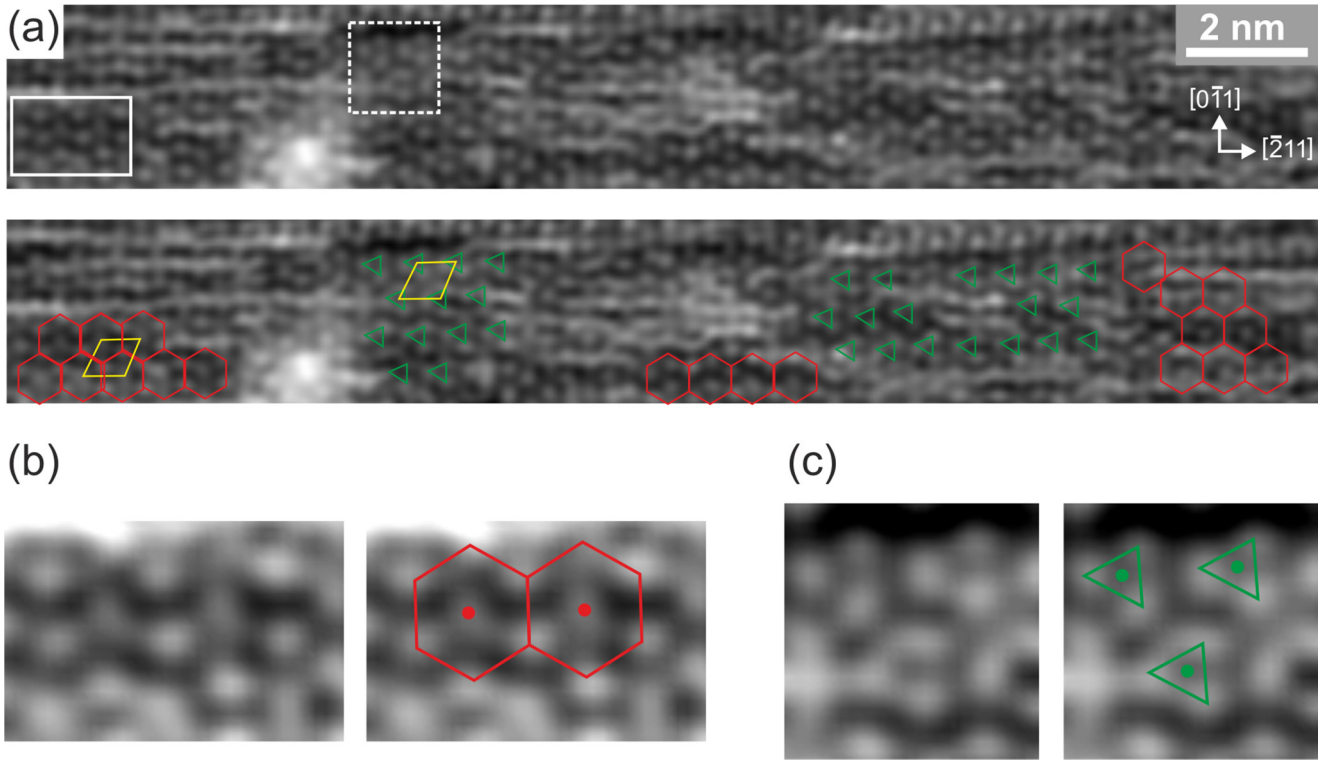

FIG. 2. STM results for 2 ML Tb on Si(111) deposited at 650 °C. (a) Detailed STM image with atomic resolution, taken at a sample voltage of +0.6 V and a tunneling current of 1 nA. Domains with two different types of structural motives can be distinguished. There is a sixfold symmetry indicated by red hexagons and a threefold symmetry indicated by green triangles, as showcased in the bottom image. (b) and (c) Magnification of the two different types of structural motives, with the position of the subsurface vacancy marked by filled circles; (b) corresponds to the solid box and (c) to the dashed box in (a).

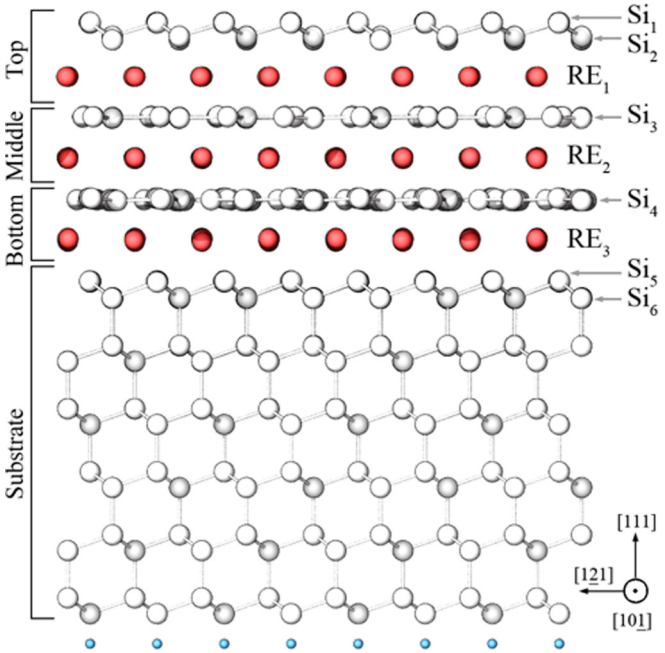

FIG. 3. Side view of the rare-earth silicide trilayer with $(2\sqrt{3} \times \sqrt{3})R30^\circ$ periodicity on the Si(111) surface. Si atoms are white, RE atoms are red, and H atoms are blue. The silicide can be thought of as a stacking of three silicide monolayers, labeled by top (Si_1 and Si_2), middle (Si_3), and bottom (Si_4). Si vacancies are distributed in the middle and bottom layers (not shown here). The topmost Si bilayer is buckled, while the Si_3 and Si_4 layers are silicene-like, with a vacancy superstructure.

in the first subsurface Si layer (see Fig. 3) [9,29–31]. Triangles correspond to the case in which the vacancies in the subsurface Si layer (Si_3) are located underneath the bottom Si atoms of the silicide surface layer (Si_2), and hexagons mean that the vacancies are located underneath the top Si atoms (Si_1). The positions of the subsurface vacancies are marked explicitly in Figs. 2(b) and 2(c) by filled circles. As observed in Fig. 2(a), these domain types alternate across the sample, and their domain sizes agree well with those deduced from the spot splitting in the SPA-LEED measurements, as will be demonstrated further below. The transition from one type of domain to the other must be accompanied by a breaking of translational symmetry due to APDBs in order to explain the splitting of diffraction spots observed in the SPA-LEED experiments.

The fact that no $(2\sqrt{3} \times \sqrt{3})R30^\circ$ but a $(\sqrt{3} \times \sqrt{3})R30^\circ$ periodicity can be observed in the STM images suggests that the subsurface layer (Si_3) has a $(\sqrt{3} \times \sqrt{3})R30^\circ$ structure, while the $(2\sqrt{3} \times \sqrt{3})R30^\circ$ structure is located in a deeper layer (Si_4). Therefore, it is more difficult to observe the $(2\sqrt{3} \times \sqrt{3})R30^\circ$ structure by STM experiments with their very high surface sensitivity as compared to that of (SPA-)LEED experiments, which also probe deeper atomic layers.

Combining the STM and (SPA-)LEED data, we assume a basic structure as shown in Fig. 3, where the topmost surface layer is composed of a buckled Si layer (Si_1,Si_2) and the first subsurface Si layer (Si_3) shows the well-known $(\sqrt{3} \times \sqrt{3})R30^\circ$ reconstruction with one Si vacancy per unit cell explaining the STM images (see Fig. 2). The second subsurface Si layer (Si_4) is composed of the $(2\sqrt{3} \times \sqrt{3})R30^\circ$ reconstruction explaining the diffraction pattern. Compared to the vacancy-induced $(\sqrt{3} \times \sqrt{3})R30^\circ$ superstructure of the Si_3 layer, the doubling of the periodicity in the Si_4 layer in one direction is achieved by doubling of the unit cell in that direction by means of adding one Si atom in every second vacancy. This model of the $(2\sqrt{3} \times \sqrt{3})R30^\circ$ reconstruction formally results in an RE_6Si_{11} stoichiometry due to the reduced density of Si vacancies in the Si_4 layer. This assumption agrees well with our AES studies (not shown here). Such a layer sequence with more rare-earth-rich silicides close to the surface and more Si-rich silicides closer to the Si substrate could be related to a diffusion-limited silicide formation.

B. Structure: Theoretical models

To verify the stability of the model proposed in the previous section, we have performed DFT calculations of a 3-ML-thick silicide film on the Si(111) surface, as shown in Fig. 3. The $(2\sqrt{3} \times \sqrt{3})R30^\circ$ superstructure has been modeled introducing an additional Si atom in every second $(\sqrt{3} \times \sqrt{3})R30^\circ$ surface unit cell, thus filling its vacancy. According to the experimental observation, the topmost Si bilayer does not host Si vacancies and is characterized by an outer buckled Si double layer. DFT calculations show that the Si bilayer—similarly to the silicide structure with $(\sqrt{3} \times \sqrt{3})R30^\circ$ periodicity—is not rotated by 180° with respect to the substrate [9,29,30,32], in contrast to the silicide monolayers with (1×1) periodicity [9,33]. The Si vacancies (V_{Si}) are distributed in the middle (Si_3) and bottom layer (Si_4). Thus a total of three V_{Si} per $(2\sqrt{3} \times \sqrt{3})R30^\circ$ surface unit cell is needed to account for the periodicity observed in the diffraction experiments. Of the three V_{Si}, either two are placed in the middle layer and one in the bottom layer or a single one is placed in the middle layer and two in the bottom layer. Thus, the silicide film consists of three silicide monolayers of different periodicity.

DFT calculations have been performed to optimize the geometry of these structures. The vacancies in the silicene-like layers labeled by Si_3 and Si_4 might occur either under atoms of the Si_1 layer or under atoms of the Si_2 layer. The two configurations have very similar formation energies in the silicide structure with $(\sqrt{3} \times \sqrt{3})R30^\circ$ periodicity [9]. Thus, many different vacancy distributions are conceivable. Let us imagine there is a bottom monolayer of $(2\sqrt{3} \times \sqrt{3})R30^\circ$ periodicity, with a single vacancy under an Si_1 atom, e.g., at the site labeled by A in Fig. 4. The two Si vacancies in the middle layer must be placed in such a way that the $(\sqrt{3} \times \sqrt{3})R30^\circ$ periodicity of the layer is preserved. This rules out most of the possible different configurations. If we consider vacancies in the middle layer under an Si_1 atom, only vacancy pairs at the lattice sites A and Δ, or E and B, or Z and Γ are possible. In the first case, vacancy channels are formed. If we consider vacancies under an Si_2 atom instead, only pairs at the lattice sites α and δ, or ε and β, or ζ and γ are possible. Thus a total of 24 different combinations are compatible with the given silicide periodicity, which are summarized in Table I together with their formation energies, given with respect to the most stable

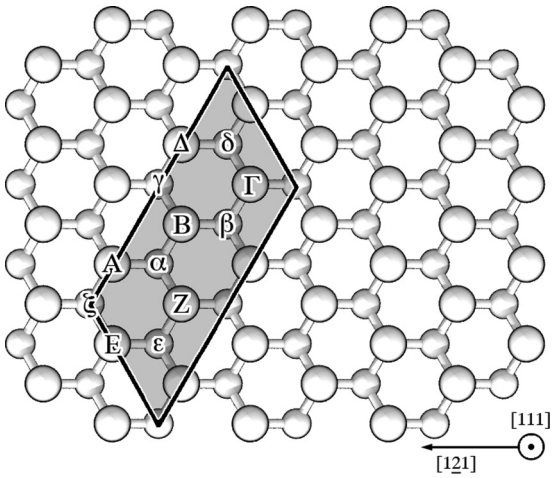

FIG. 4. Top view of the trilayer RE silicide with $(2\sqrt{3}\times\sqrt{3})R30^\circ$ periodicity on the Si(111) surface. Atoms of the topmost Si bilayer correspond to the layers Si_1 (larger circles) and Si_2 (smaller circles). RE atoms in the center of the hexagons are not shown, and the Si atoms in the deeper Si_3 and Si_4 layers are hidden below the Si_1 and Si_2 atoms. The surface unit cell is highlighted.

models (models e/f). Symmetry reasons reduce the number of nonequivalent configurations to 16. Some configurations, labeled by *Unstable*, relax without any barrier into other structural models. Our calculations reveal that the investigated $(2\sqrt{3}\times\sqrt{3})R30^\circ$ silicide structures, similarly to the observed silicide phases with $(2\sqrt{3}\times 2\sqrt{3})R30^\circ$ or (5×2)

TABLE I. Relative formation energies E_{form} (in eV per $(2\sqrt{3}\times\sqrt{3})R30^\circ$ unit cell) and average Si-Si distances (d_{Si} in Å) in the silicene-like layers Si_3 and Si_4 for the case of Tb. $d_{\%}$ labels the deviations (in %) from the Si-Si distance in bulk Si (2.352 Å).

Model	V_{Si} in Si_3	V_{Si} in Si_4	E_{form}	d_{Si} in Si_3,Si_4	$d_{\%}$
a	α	α,δ	0.656	2.350, 2.439	1.81
b	α	ε,β	0.491	2.341, 2.428	1.40
c	α	ζ,γ	0.491	2.341, 2.428	1.40
d	α,δ	α	0.218	2.415, 2.434	1.38
e	ε,β	α	0.000	2.404, 2.349	1.04
f	ζ,γ	α	0.000	2.404, 2.349	1.04
g	α	A,Δ	0.343	2.344, 2.423	1.34
h	α	E,B	0.343	2.344, 2.423	1.34
i	α	Z,Γ	0.343	2.344, 2.423	1.34
j	A,Δ	α	Unstable		
k	E,B	α	Unstable		
l	Z,Γ	α	Unstable		
m	A	A,Δ	0.449	2.352, 2.426	1.58
n	A	E,B	0.287	2.347, 2.421	1.37
o	A	Z,Γ	0.287	2.347, 2.421	1.37
p	A,Δ	A	0.302	2.434, 2.353	1.77
q	E,B	A	0.094	2.425, 2.350	1.52
r	Z,Γ	A	0.094	2.425, 2.350	1.52
s	A	α,δ	0.547	2.352, 2.430	1.65
t	A	ε,β	0.547	2.352, 2.430	1.65
u	A	ζ,γ	Unstable		
v	α,δ	A	Unstable		
w	ε,β	A	Unstable		
x	ζ,γ	A	Unstable		

periodicity [9], are metastable. A common feature of the investigated models is that the energetically favored position for the layer with the $(2\sqrt{3}\times\sqrt{3})R30^\circ$ periodicity is always the bottom layer, while the layer with the $(\sqrt{3}\times\sqrt{3})R30^\circ$ periodicity is always formed as the middle layer, independent of the particular arrangement of the vacancies.

Another common feature is that the vacancies in the middle layer are not formed on top of vacancies in the bottom layer. In other words, vertical vacancy channels are energetically unfavorable. In the energetically most stable configuration (model *e*), the vacancies are formed in both layers under the Si_2 atoms. However, a model in which the vacancies in both layers are formed below the Si_1 atoms (model *r*) is less stable by only 47 meV per $(\sqrt{3}\times\sqrt{3})R30^\circ$ unit cell. On the one hand, this confirms the results of previous theoretical studies [9,29,30,32,34], which pointed out that in silicide layers with $(\sqrt{3}\times\sqrt{3})R30^\circ$ periodicity the Si vacancies under Si_1 and Si_2 are characterized by very similar formation energies ($\Delta E \sim 50$ meV). On the other hand, this small energy difference, in the order of the thermal energies during silicide formation of ~80 meV, explains the coexistence of different domains with $(2\sqrt{3}\times\sqrt{3})R30^\circ$ periodicity. These can indeed be interpreted as silicide regions with vacancies below Si_1 and below Si_2 atoms. The trilayer structure of the film with $(2\sqrt{3}\times\sqrt{3})R30^\circ$ periodicity is very similar to the bilayer structure of the film with $(\sqrt{3}\times\sqrt{3})R30^\circ$ periodicity, with an additional monolayer in which every second Si vacancy is missing. In this layer (Si_4 in Fig. 3), the Si atoms do not relax symmetrically toward the vacancy as in the case of the structure with $(\sqrt{3}\times\sqrt{3})R30^\circ$ periodicity. Indeed, as the threefold rotational symmetry is broken in the $(2\sqrt{3}\times\sqrt{3})R30^\circ$ structure, a Si vacancy has (in the direction of the first Si neighbors) one vacancy in a distance of 6.70 Å and two equivalent vacancies at 13.39 Å. Thus, two atoms in the Si_4 layer relax by 0.681 Å, while the Si atom in the direction of the shorter vacancy distance relaxes toward the vacancy by 0.379 Å.

Simulated constant-height STM images of the energetically stable structure of the silicide are calculated within the Tersoff-Hamann model [35,36]. The results of the calculations performed for the model *r* with Si vacancies under Si_1 atoms are shown in Figs. 5(a) and 5(c) for filled and empty states, respectively. The simulated STM images show a hexagonal pattern consisting of darker and brighter spots with the sixfold $p6$ symmetry. The darker spots are assigned to Si_1 atoms above an Si vacancy in the middle layer. Thus, the simulated STM images are nearly identical with the corresponding STM images simulated for the silicide with $(\sqrt{3}\times\sqrt{3})R30^\circ$ periodicity, which are shown for comparison in Figs. 5(b) and 5(d). The calculations for model *e* with Si vacancies under Si_2 atoms are shown in Figs. 5(e) and 5(g) for filled and empty states, respectively. The threefold $p3$ symmetry is reflected in the small lateral undulation of the Si_1 atoms highlighted by the dashed green lines and arrows. Again, the simulated STM images are nearly identical to the corresponding STM images simulated for the silicide with $(\sqrt{3}\times\sqrt{3})R30^\circ$ periodicity, as shown in Figs. 5(f) and 5(h).

All patterns are in very good agreement with previous calculations performed within the same approach [9,29,30,32,34]. In conclusion, Fig. 5 clearly shows that the silicide structures with $(2\sqrt{3}\times\sqrt{3})R30^\circ$ and $(\sqrt{3}\times\sqrt{3})R30^\circ$ periodicity are

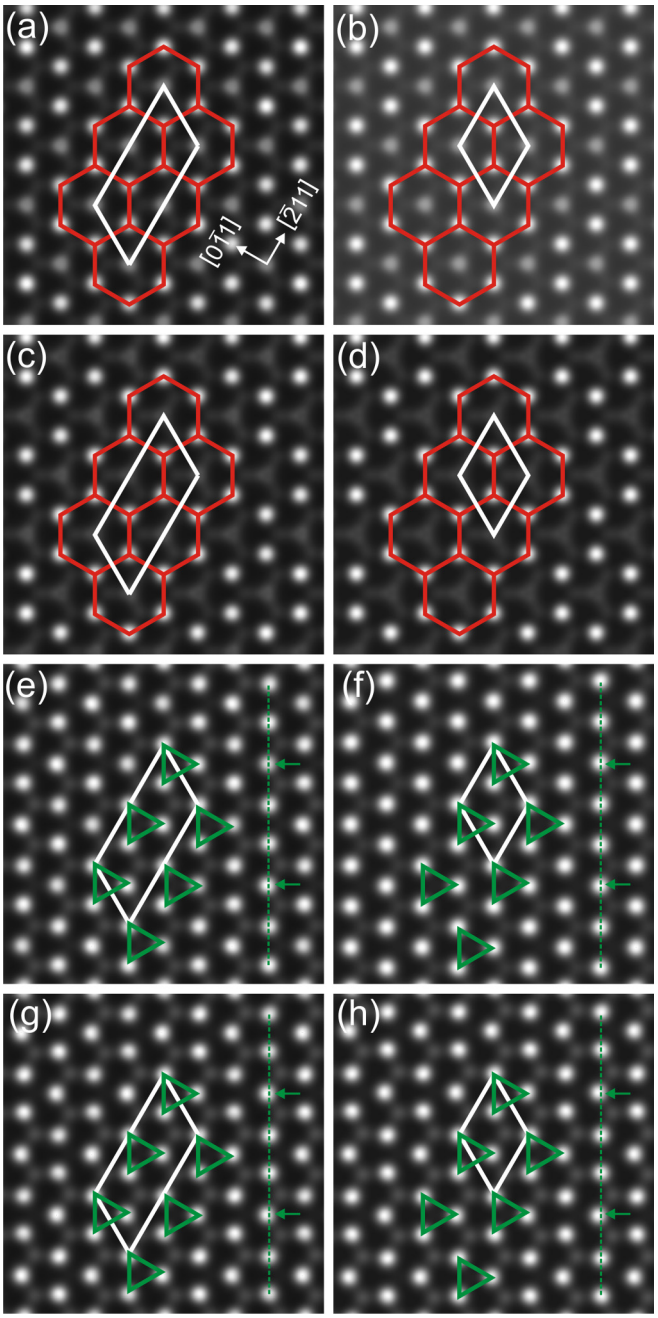

FIG. 5. (a), (c), (e), and (g) Simulated STM images of the trilayer Tb silicide with $(2\sqrt{3} \times \sqrt{3})R30^\circ$ periodicity (models *r*,*e*). Filled states are shown in (a) and (e), while empty states are shown in (c) and (g), respectively. The simulations for the bilayer RE silicide with $(\sqrt{3} \times \sqrt{3})R30^\circ$ periodicity are shown for comparison in the column on the right-hand side [(b), (d), (f), and (h)]. Calculations are performed for tunneling voltages of ± 0.3 V.

indistinguishable in STM investigations. This explains why the silicide phase with $(2\sqrt{3} \times \sqrt{3})R30^\circ$ periodicity is only visible in electron diffraction experiments, which are able to collect information from deeper atomic layers below the surface, while it is not visible in STM experiments, which are dominated by the outmost surface layers.

The presence of vacancies in the silicide thin films with $(\sqrt{3} \times \sqrt{3})R30^\circ$ periodicity has been explained as a mechanism to release the compressive strain in the silicene-like layer formed between the RE planes [33]. The same argument holds true for the silicide phase with $(2\sqrt{3} \times \sqrt{3})R30^\circ$ periodicity. The calculated next-neighbor distance d_{Si} for free-standing bulk Si is 2.352 Å. In an ideal, vacancy-free silicene layer, d_{Si} amounts to 2.232 Å (within DFT-PBE), resulting in a large compressive strain of about 5.4%. Through the presence of Si vacancies, this strain can be released. Indeed, the average d_{Si} value in the $(2\sqrt{3} \times \sqrt{3})R30^\circ$ phase is 2.378 Å (for model *e*), very close to the bulk value. Interestingly, the most stable models are the models for which the average d_{Si} is very close to the bulk value.

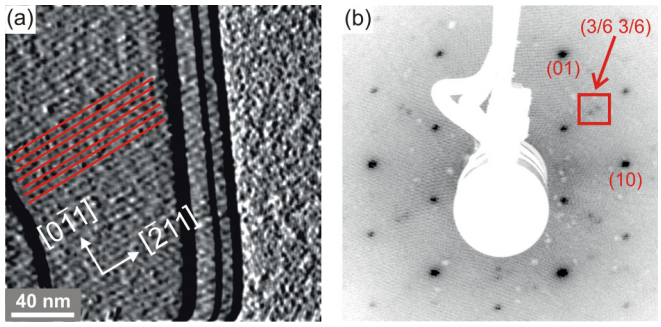

FIG. 6. (a) Overview STM image, taken at a sample voltage of +2.0 V and a tunneling current of 50 pA. After the application of a gradient filter, a striped structure can be observed on the terraces. Red lines indicate domains of the same type. (b) Conventional LEED image of the same sample taken at an electron energy of 100 eV ($\equiv S = 6.77$) exhibiting the characteristic splitting of the third-order $(2\sqrt{3} \times \sqrt{3})R30^\circ$ diffraction spots.

C. Antiphase domain boundaries

Large-scale STM images, as shown in Fig. 6(a), show a striped quasi-one-dimensional structure. Due to the fact that the diffraction pattern is split in $2\sqrt{3}$ direction, as observed in the experimental (SPA-)LEED patterns in Figs. 1 and 6(b), it has to be concluded that the striped domains are oriented along the $\sqrt{3}$ direction. Along the stripes, the growth is only limited by step edges, whereas in the $2\sqrt{3}$ direction the distance between two similar domains is reflected in the magnitude of the spot splitting observed in the SPA-LEED experiments. Reversely, this means that the transition from one type of domain to the other must be accompanied by a breaking of translational symmetry in the $2\sqrt{3}$ direction causing the APDBs.

Unfortunately, the (atomic) structure of the APDBs could not be resolved in our STM experiments. However, based on our DFT calculations and STM images, we assume that domains with Si_3 vacancies under Si_2 atoms (*e* or *f* domains) alternate with domains with Si vacancies under Si_1 atoms (*q* or *r*). In addition, due to the splitting of odd-order diffraction spots and no splitting of even-order diffraction spots, it is mandatory that the sum of the widths of two adjacent APDBs is an odd multiple of $a_0\sqrt{3}$, with $a_0 = 3.840$ Å being the Si(111) surface lattice constant. Additionally, strain reduction seems to play an integral role in the formation of this structure, hence also in the formation of the APDBs. As already mentioned before, the strain can be quantified by the mean next-neighbor distance d_{Si} in the silicene-like layers compared

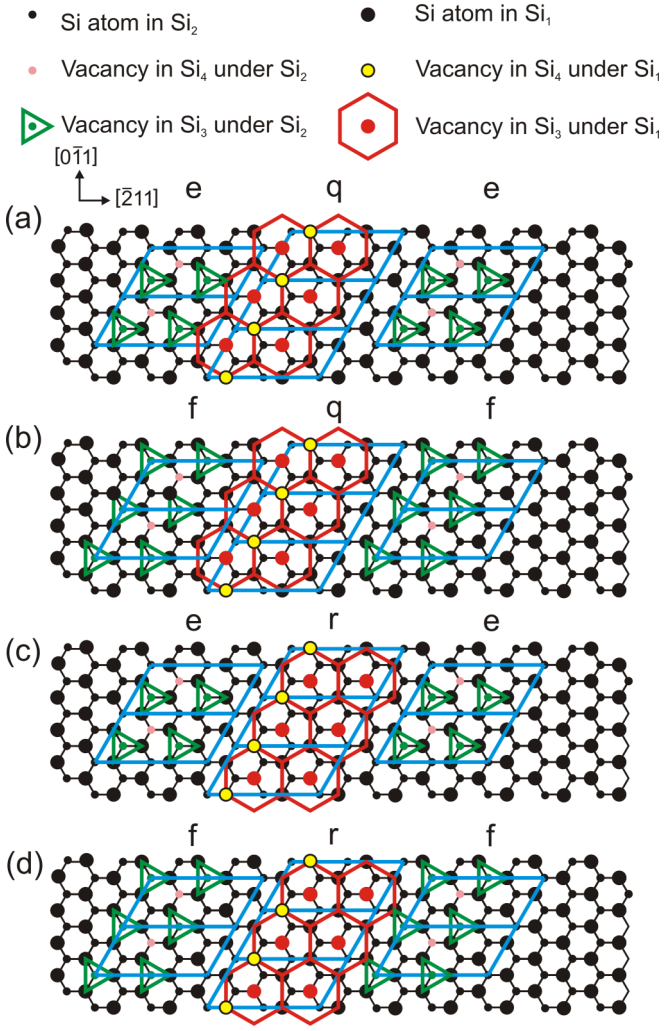

FIG. 7. (a)–(d) Schematic display of the four models discussed in the text (RE atoms were omitted for the sake of clarity). The width of one of the APDBs is $1/3 \times a_0\sqrt{3}$ and the width of the other one is $2/3 \times a_0\sqrt{3}$, resulting in the mandatory sum of $a_0\sqrt{3}$ for both APDBs in the supercell. Note that the stripes displayed here are only one unit cell wide, while they are wider in reality. The corresponding diffraction patterns are shown in Fig. 8(a).

to the d_{Si} in bulk Si. The most stable models (e,f) and (r,q) overcompensate the strain by 1.04% and 1.52%, respectively. This suggests that the APDBs will contain no Si vacancies to account for this overcompensation. Due to the small misfit, it is also to be expected that the APDBs will be as narrow as possible, with the sum of the widths amounting to $a_0\sqrt{3}$.

Due to the inequalities of the domains, there are APDBs that have a width of $1/3 \times a_0\sqrt{3}$ ($\mathrm{APDB}_{1/3}$) and APDBs that have a width of $2/3 \times a_0\sqrt{3}$ ($\mathrm{APDB}_{2/3}$). Moreover, both types of APDBs alternate. As shown schematically in Fig. 7, this leads to the following structure of the supercell (only considering the most energetically favorable models):

$$[\gamma_1(e,f) \,||\, \mathrm{APDB}_{1/3} \,||\, \gamma_2(q,r) \,||\, \mathrm{APDB}_{2/3}], \qquad (1)$$

describing the quasi-one-dimensional structure. γ_1 and γ_2 are the number of $(2\sqrt{3} \times \sqrt{3})R30^\circ$ unit cells of the respective domains (e,f) and (q,r).

To test this assumption, we simulate line profiles of different diffraction peaks employing the binary surfaces technique [37] using a 4096×1 lattice with periodic boundary conditions. The respective lattice periodicities are $1/3 \times a_0\sqrt{3}$ in one direction and $a_0\sqrt{3}$ in the other direction in order to realize the APDBs as well as the striped $(2\sqrt{3} \times \sqrt{3})R30^\circ$ domains. The sequence of the different types of domains and APDBs are chosen in accordance with the proposed structure models (see Fig. 7). The domains and APDBs are described by their sequence of Si atoms and vacancies in the Si_3 and Si_4 layers, since the rest of the structure (RE layers and buckled Si layer Si_1,Si_2) exhibits a 1×1 periodicity, and thus does not influence the line shape of the split spots. Considering only the four most stable models (e, f, q, and r), we assume that the fraction c of each of the two different types of structural units (e,f and q,r) is given by [38]

$$c_i = \frac{Z_i}{Z} \text{ with } Z = \sum_i Z_i \text{ and } Z_i = g_i \exp\left[-\frac{E_{\mathrm{form},i}}{k_B T}\right], \quad (2)$$

where k_B is the Boltzmann constant, T is the temperature, and g_i is the symmetry-dependent degeneracy factor. All models exhibit an oblique Bravais lattice

$$a = a_0 2\sqrt{3} \neq b = a_0\sqrt{3}, \quad \measuredangle \neq 90^\circ, \qquad (3)$$

with the lattice vectors a,b, with no twofold rotational axes, due to the involved four Si layers of the unit cell, resulting in the plane crystallographic group $p1$. Therefore, the symmetry-dependent degeneracy factor g_i is equal for all models and can be omitted in the case at hand. For the preparation temperature of $T = 923$ K (650 °C) and taking into account the formation energies E_{form} presented in Table I, this equates to $c_{e,f} = 0.77$ and $c_{q,r} = 0.23$, meaning that the mean domain size $\langle\gamma_{e,f}\rangle$ of models e,f should be thrice as high as the mean domain size $\langle\gamma_{q,r}\rangle$ of the models q,r. The size of both domains γ_i follows the Gamma distribution [39]

$$P_i(\gamma_i) \propto \left(\frac{M_i\gamma_i}{\langle\gamma_i\rangle}\right)^{M_i-1} \exp\left[-\frac{M_i\gamma_i}{\langle\gamma_i\rangle}\right]. \qquad (4)$$

Here, $\langle\gamma_i\rangle$ denotes the average domain size of the Gamma distribution, and the parameter M_i, which is assumed to be identical for both types of models (e,f and q,r), depends on its standard deviation σ_i via $M_i = (\langle\gamma_i\rangle/\sigma_i)^2$.

The width of the respective domain is determined by Gamma-distributed random numbers following the Gamma distribution described above. Subsequently, the absolute square of the Fourier transform, which can be interpreted as the diffraction pattern (kinematic approximation), is computed. This process is repeated 2048 times in order to simulate the incoherent superposition of different regions in LEED experiments. The line profiles are averaged and thus the simulated line profile I_{sim} is obtained.

First, the four different models shown in Fig. 7 will be discussed. Here, only one type of supercell is repeated [e.g., e and q for Fig. 7(a)]. The results of the simulations for the four models (see Fig. 7) are shown in Fig. 8(a). For the models ($e \leftrightarrow q$) and ($f \leftrightarrow r$) [see Figs. 7(a) and 7(d)], the splitting of only odd-order diffraction spots is reproduced. Depending on the out-of-plane momentum, the diffraction spots are split asymmetrically [see Fig. 8(a)]. This is in good agreement with

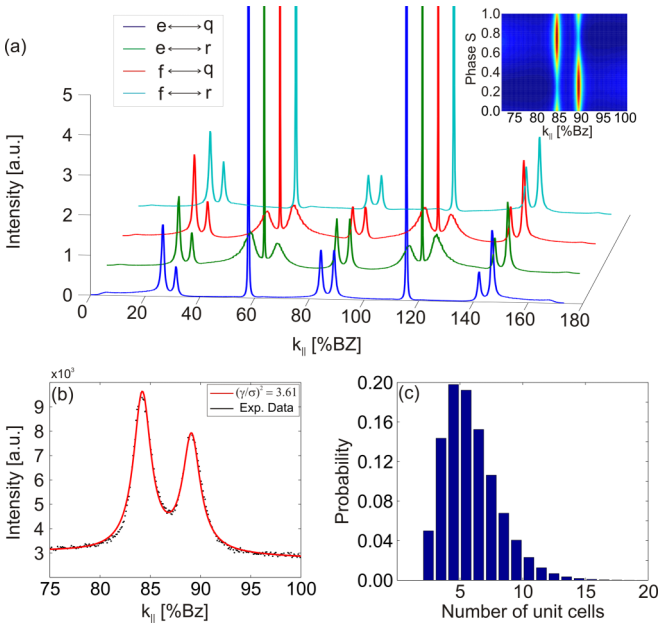

FIG. 8. (a) Simulated diffraction patterns of the four different APDB models [at in-phase conditions $S \in \mathbb{N}$] shown in Fig. 7 and simulated reciprocal space map of the third-order diffraction spot showing an undulation of the intensity ratio of the split peaks as a function of out-of-plane momentum. This very undulation can be observed experimentally in Fig. 1, in which the split spots exhibit intensity undulations when the electron energy is varied. The in-plane momentum is given in %Bz, where $100\%\mathrm{Bz} \equiv \frac{2\pi}{a_0 \cos(30^\circ)} = 1.89\ \text{Å}^{-1}$, and the out-of-plane momentum is given by the scattering phase S. (b) Simulated split third-order diffraction spot (red) obtained by minimization of the mean-squared error (see the text) compared with the experimental data for Dy (black) showing very good agreement. (c) Resulting domain-size distribution for the supercell in units of $a_0 2\sqrt{3}$.

the experimental data [see Figs. 1(a)–1(c) and 6(b)], which also shows asymmetrically split spots at certain points of the reciprocal space. Thus the simulated diffraction patterns of both models agree very well with the experimental data.

In contrast, the models ($e \leftrightarrow r$) and ($f \leftrightarrow q$) [see Figs. 7(b) and 7(c)] exhibit an additional splitting of even-order diffraction spots, as shown in Fig. 8(a). Due to the fact that no such splitting can be observed in the experimental diffraction patterns, this means that the probability of formation of the transitions ($e \leftrightarrow q$) and ($f \leftrightarrow r$) must be significantly higher than the probability of formation of the transitions ($e \leftrightarrow r$) and ($f \leftrightarrow q$). Unfortunately, this assumption cannot be tested by means of DFT calculation due to the rather large supercells.

This difference in formation probability rules out a statistical mixing of the four different types of supercells as well. As a matter of fact, the simulated diffraction patterns of these statistically mixed supercells (not shown here) all exhibit very broad even-order diffraction spots (due to the merging of split and nonsplit even order spots), which is in stark contrast to the experimental data.

To be able to compare the simulated diffraction peak profiles I_{sim} quantitatively with the experimental diffraction peak profiles I_{exp} and to determine the domain-size distribution, the simulated profiles have to be convoluted with the instrument function I_{inst} [40]. This instrument function is deduced from the nonsplit even-order superstructure spots of the experimental diffraction pattern, because these peaks are insensitive to the influence of APDBs on the line shape. After convolution, the mean-squared error describing the deviation from the experimental data is computed varying both the average domain size and the standard deviations ($\langle\gamma_{e,f}\rangle$,$\sigma_{e,f}$) until the mean-squared error is minimized. The result is shown in Fig. 8(b), and a domain-size distribution with the average domain size $\langle\gamma_{e,f}\rangle = 3.99$ and a standard deviation $\sigma_{e,f} = 2.10$ is derived for the models (e,f), which equates to an average domain size $\langle\gamma_{q,r}\rangle = 1.33$ and a standard deviation $\sigma_{q,r} = 0.70$ for the models (q,r). In addition, we would like to mention that these numerical results agree well with results obtained calculating diffraction spot profiles within the context of the domain matrix method [41–43].

The magnitude of the splitting observed in the diffraction pattern is caused by the average size of the supercell, for which the domain-size distribution is shown in Fig. 8(c), i.e., the average distance between two domains of the same type, resulting in a $\langle\gamma\rangle_{\text{tot}} = \langle\gamma_{e,f}\rangle + \langle\gamma_{q,r}\rangle + 1/6 + 2/6 = 5.82$ and a total standard deviation of $\sigma_{\text{tot}} = \sqrt{\sigma_{e,f}^2 + \sigma_{q,r}^2} = 2.21$. Because of the unit-cell width of $2a_0\sqrt{3} = 1.33$ nm, this corresponds to a periodicity of 7.74 nm, in good agreement with the results of the STM experiments yielding ∼8 nm.

IV. CONCLUSION

Using (SPA-)LEED, STM, DFT, and kinematic diffraction calculations, we were able to detect and structurally resolve a formerly unknown $(2\sqrt{3} \times \sqrt{3})R30^\circ$ reconstruction, which is observed after evaporation of the REEs Dy and Tb on Si(111) at elevated temperatures. The experimental data can be explained by a structure model, which is derived from the structure of the similar $(\sqrt{3} \times \sqrt{3})R30^\circ$ reconstruction. The annihilation of vacancies due to the addition of Si atoms in the deeper Si layer causes a lateral uniaxial strain, which induces quasi-one-dimensional striped domains separated by APDBs. The average width of the supercell (consisting of two different domains) derived from the SPA-LEED spot splitting amounts to 5.82 $(2\sqrt{3} \times \sqrt{3})R30^\circ$ unit cells. We assume that the domain boundaries are formed to reduce the lateral strain.

ACKNOWLEDGMENTS

The authors would like to thank the Deutsche Forschungsgemeinschaft for financial support through FOR 1700, projects E2 and T1.

[1] J. E. Baglin, F. M. d'Heurle, and C. S. Petersson, Appl. Phys. Lett. **36**, 594 (1980).

[2] K. N. Tu, R. D. Thompson, and B. Y. Tsaur, Appl. Phys. Lett. **38**, 626 (1981).

[3] J. A. Knapp and S. T. Picraux, Appl. Phys. Lett. **48**, 466 (1986).
[4] F. P. Netzer, J. Phys. Condens. Matter **7**, 991 (1995).
[5] C. Preinesberger, S. Vandré, T. Kalka, and M. Dähne-Prietsch, J. Phys. D **31**, L43 (1998).
[6] Y. Chen, D. A. A. Ohlberg, G. Medeiros-Ribeiro, Y. A. Chang, and R. S. Williams, Appl. Phys. Lett. **76**, 4004 (2000).
[7] G. S. Snider and R. S. Williams, Nanotechnology **18**, 035204 (2007).
[8] D. E. Chang, A. S. Sørensen, P. R. Hemmer, and M. D. Lukin, Phys. Rev. Lett. **97**, 053002 (2006).
[9] S. Sanna, C. Dues, W. G. Schmidt, F. Timmer, J. Wollschläger, M. Franz, S. Appelfeller, and M. Dähne, Phys. Rev. B **93**, 195407 (2016).
[10] M. Franz, J. Große, R. Kohlhaas, and M. Dähne, Surf. Sci. **637-638**, 149 (2015).
[11] T. P. Roge, F. Palmino, C. Savall, J. C. Labrune, and C. Pirri, Surf. Sci. **383**, 350 (1997).
[12] C. Battaglia, H. Cercellier, C. Monney, M. G. Garnier, and P. Aebi, Europhys. Lett. **77**, 36003 (2007).
[13] A. Kirakosian, J. L. McChesney, R. Bennewitz, J. N. Crain, J.-L. Lin, and F. J. Himpsel, Surf. Sci. **498**, L109 (2002).
[14] E. W. Perkins, I. M. Scott, and S. P. Tear, Surf. Sci. **578**, 80 (2005).
[15] I. Engelhardt, C. Preinesberger, S. K. Becker, H. Eisele, and M. Dähne, Surf. Sci. **600**, 755 (2006).
[16] S. Vandré, C. Preinesberger, W. Busse, and M. Dähne, Appl. Phys. Lett. **78**, 2012 (2001).
[17] G. Kresse and J. Furthmüller, Comput. Mater. Sci. **6**, 15 (1996).
[18] G. Kresse and J. Furthmüller, Phys. Rev. B **54**, 11169 (1996).
[19] J. P. Perdew, J. A. Chevary, S. H. Vosko, K. A. Jackson, M. R. Pederson, D. J. Singh, and C. Fiolhais, Phys. Rev. B **46**, 6671 (1992).
[20] J. P. Perdew, K. Burke, and M. Ernzerhof, Phys. Rev. Lett. **77**, 3865 (1996).
[21] P. E. Blöchl, Phys. Rev. B **50**, 17953 (1994).
[22] G. Kresse and D. Joubert, Phys. Rev. B **59**, 1758 (1999).
[23] V. I. Anisimov, F. Aryasetiawan, and A. I. Lichtenstein, J. Phys.: Condens. Matter **9**, 767 (1997).
[24] S. Sanna, W. G. Schmidt, T. Frauenheim, and U. Gerstmann, Phys. Rev. B **80**, 104120 (2009).
[25] S. Sanna, T. Frauenheim, and U. Gerstmann, Phys. Rev. B **78**, 085201 (2008).
[26] H. J. Monkhorst and J. D. Pack, Phys. Rev. B **13**, 5188 (1976).
[27] J. Neugebauer and M. Scheffler, Phys. Rev. B **46**, 16067 (1992).
[28] L. Bengtsson, Phys. Rev. B **59**, 12301 (1999).
[29] T. P. Roge, F. Palmino, C. Savall, J. C. Labrune, P. Wetzel, C. Pirri, and G. Gewinner, Phys. Rev. B **51**, 10998 (1995).
[30] J. A. Martín-Gago, J. M. Gómez-Rodríguez, and J. Y. Veuillen, Surf. Sci. **366**, 491 (1996).
[31] C. Rogero, J. A. Martín-Gago, and J. I. Cerdá, Phys. Rev. B **74**, 121404(R) (2006).
[32] J. A. Martín-Gago, J. M. Gómez-Rodríguez, and J. Y. Veuillen, Phys. Rev. B **55**, 5136 (1997).
[33] L. Stauffer, A. Mharchi, C. Pirri, P. Wetzel, D. Bolmont, G. Gewinner, and C. Minot, Phys. Rev. B **47**, 10555 (1993).
[34] P. Wetzel, S. Saintenoy, C. Pirri, D. Bolmont, G. Gewinner, T. P. Roge, F. Palmino, C. Savall, and J. C. Labrune, Surf. Sci. **355**, 13 (1996).
[35] J. Tersoff and D. R. Hamann, Phys. Rev. Lett. **50**, 1998 (1983).
[36] J. Tersoff and D. R. Hamann, Phys. Rev. B **31**, 805 (1985).
[37] F. Klasing, Ph.D. thesis, University Duisburg-Essen, 2014.
[38] O. Romanyuk, F. Grosse, A. Proessdorf, W. Braun, and H. Riechert, Phys. Rev. B **82**, 125315 (2010).
[39] J. Wollschläger, Surf. Sci. **383**, 103 (1997).
[40] M. Henzler, in *Dynamical Phenomena at Surfaces, Interfaces and Superlattices*, edited by F. Nizzoli, K.-H. Rieder, and R. F. Willis, Springer Series in Surface Sciences Vol. 3 (Springer, Berlin, 1985), pp. 20–24.
[41] J. E. Houston and R. L. Park, Surf. Sci. **21**, 209 (1970).
[42] S. Pflanz and W. Moritz, Acta Crystallogr. A **48**, 716 (1992).
[43] J. Wollschläger, Surf. Sci. **328**, 325 (1995).